Ciliopathy genes are required for apical secretion of Cochlin, an otolith crystallization factor

Eleni Leventea[a], Zhou Zhu[a,1], Xiaoming Fang[a,1], Yulia Nikolaeva[a], Eleanor Markham[a], Robert A. Hirst[b], Fredericus J. M. van Eeden[a,2], and Jarema J. Malicki[a]

[a]Department of Biomedical Science, University of Sheffield, Sheffield S10 2TN, United Kingdom; and [b]Department of Respiratory Sciences, University of Leicester, Leicester LE1 7RH, United Kingdom

Edited by Iain A. Drummond, Mount Desert Island Biological Laboratory, Bar Harbor, ME, and accepted by Editorial Board Member Stephen T. Warren May 28, 2021 (received for review February 10, 2021)

Here, we report that important regulators of cilia formation and ciliary compartment–directed protein transport function in secretion polarity. Mutations in cilia genes *cep290* and *bbs2*, involved in human ciliopathies, affect apical secretion of Cochlin, a major otolith component and a determinant of calcium carbonate crystallization form. We show that Cochlin, defective in human auditory and vestibular disorder, DFNA9, is secreted from small specialized regions of vestibular system epithelia. Cells of these regions secrete Cochlin both apically into the ear lumen and basally into the basal lamina. Basally secreted Cochlin diffuses along the basal surface of vestibular epithelia, while apically secreted Cochlin is incorporated into the otolith. Mutations in a subset of ciliopathy genes lead to defects in Cochlin apical secretion, causing abnormal otolith crystallization and behavioral defects. This study reveals a class of ciliary proteins that are important for the polarity of secretion and delineate a secretory pathway that regulates biomineralization.

cep290 | Cochlin | ear | apical secretion | otolith

Cilia are finger-like cell surface protrusions involved in an immense array of biological processes that range from limb patterning in the embryo to light detection in the eye. Numerous cilia genes are associated with human disorders collectively known as ciliopathies. While analyzing cilia function in vertebrate sensory organs, we focused on Cep290, a protein that localizes to centrosomes and the ciliary transition zone. Human *CEP290* defects range from blindness to severe developmental defects causing perinatal lethality (1, 2). Otoliths are highly mineralized bodies that rest on the surface of sensory epithelia in the vestibular system of vertebrates. Otolith displacement that occurs in response to body movements stimulates mechanosensitive hair cells embedded in sensory epithelia, providing the organism with information about body position (3). The main inorganic component of the otolith is calcium carbonate ($CaCO_3$). Its crystal form (polymorph) varies across species and in different otolithic organs. Otolith calcium carbonate crystal form is controlled by proteinaceous matrix that remains poorly characterized and which is thought to control the balance between calcite, vaterite, and aragonite (4). In teleost fish, the utricular otolith mainly contains aragonite, the latter can be detected by Meigen's Cobalt Nitrate stain (5–7). Defects in certain otolith matrix proteins lead to the appearance of other calcium carbonate polymorphic forms and abnormal crystal morphology (6). In humans and animals, this is likely to affect vestibular function and result in behavioral defects (8, 9).

Materials and Methods

Zebrafish Strains and Maintenance. All animal studies were performed in accordance with the UK Home Office regulations and the UK Animals (Scientific Procedures) Act 1986. The *cep290*^{sa1383}, *bbs2*^{sa2952}, and *bbs9*^{sa14425} alleles were obtained from the Sanger Institute TILLING project. The *ovl*^{tz288b} allele was previously used for cilia analysis by us (10). Cochlin mutants were generated using the CRISPR/ Cas9 system, with guide RNAs targeting exons 11 and 12 (CCATGCCCAGTTGGTTCAGCACC for von Willebrand Factor 1 [vWF1] and GGCGATGGCGTCTGAGCCCAAGG for von Willebrand Factor 2 [vWF2]). To generate *cochlin* crispants, four guides were injected against exon 2 (CTTCATTAACCATGTCGTTG), exon 3 (CAGGTATTCTCTCTTTGAGC), and 2× exon 4 (GTTGCAACGCCGATTAGCTG, TATGCGGAGCAGCCATTCAC). Genotypes were determined by finclipping adult fish, followed by DNA isolation, PCR amplification of mutation sites, and Sanger sequencing. Genotyping primers are provided in Table 1. Phenotypic analysis was performed by comparing homozygous mutants and heterozygous or wild-type animals derived from the same ancestral line. For phenotypic analysis, crosses were repeated at least twice. Heat-shock promoter–driven *Arl13-b-EGFP-Inp54*^{D281A} transgenic line was used to visualize cilia. To activate expression, transgenic animals were heat shocked at 4.5 d postfertilization (dpf) for 30 min at 39 °C and fixed 12 h later. Expression was analyzed on cryosections as described in the section *Immunohistochemistry*.

Behavioral Analysis. For swimming behavior assay, 5-dpf larvae were placed in wells of a standard 24-well dish each filled with 1 mL E3 medium and left to acclimatize for 30 min in the Zebrabox chamber (ViewPoint Behavior Technology). Stress response of larvae was tested by modifying a previous protocol (11): a drop of 4 M NaCl was added to each well, resulting in the final concentration of roughly 250 mM NaCl. Following 10 min incubation, the NaCl solution was replaced with fresh E3 medium for the remainder of the assay. Swimming behavior of larvae (total distance, duration of movement, inactive time, and speed) was tracked for 10 min after E3 replacement using the Zebralab software. High (magenta, >10 mms^{-1}), medium (green), and low speed (black, <3 mms^{-1}) were annotated. Approximately 12 heterozygous and 12 mutant larvae were tested in parallel in each experiment.

Adult zebrafish behavior was recorded using the same Zebrabox tracking system and software (viewpoint behavior technology). Adult zebrafish, ~3 mo of age, were placed in beakers filled with 300 mL aquarium water and

Significance

We found that genes associated with human ciliopathies modulate apicobasal polarity of secretion. In addition, we showed that this is essential for the function of Cochlin, the protein associated with DFNA9, a human nonsyndromic deafness with vestibular dysfunction. Cochlin is secreted by a group of specialized epithelial cells both apically and basally in the ear. We found that apically secreted Cochlin is essential for proper otolith formation. In this way, we offer a plausible molecular explanation as to why DFNA9 patients suffer from balance disorders. The involvement of cilia genes in polarized secretion is an additional function for this otherwise very well-studied and medically important group of genes.

Author contributions: E.L., Z.Z., X.F., R.A.H., F.J.M.v.E., and J.J.M. designed research; E.L., Z.Z., X.F., Y.N., E.M., R.A.H., F.J.M.v.E., and J.J.M. performed research; E.L., Z.Z., X.F., E.M., R.A.H., and J.J.M. analyzed data; and E.L., F.J.M.v.E., and J.J.M. wrote the paper.

The authors declare no competing interest.

This article is a PNAS Direct Submission. I.A.D. is a guest editor invited by the Editorial Board.

[1]Z.Z. and X.F. contributed equally to this work.

[2]To whom correspondence may be addressed. Email: f.j.vaneeden@sheffield.ac.uk.

This article contains supporting information online at https://www.pnas.org/lookup/suppl/doi:10.1073/pnas.2102562118/-/DCSupplemental.

Published July 8, 2021.

Table 1. Genotyping primers

Gene	Forward	Reverse
cep290^{sa1383}	CAAGGATCTTCAGAGGAGCC	CATGACCTTAACCATTCACAGTAC
bbs2^{sa2952}	GGGAAACCTTATGGACTCAAGC	CATGTCTAACCTTGGCATTTTCCTC
bbs9^{sa1425}	TTTCCATATGTATGGTTTTCTCAGGCACCG	CGATTACCTGTAACACCACCGAATG
coch^{sh536}	GTGTGAACCTCTGACTCTCC	CATCTGATCGATGGAGC
coch^{sh555}	GAATCACTGTTTACGCAGTGG	TGCACTCAAGAAAATCTCAAAATTGTC

were acclimatized for 1 h in the Zebrabox chamber. Swimming activity was tracked for 10 min with constant light at 15% intensity inside the tracking chamber High (magenta, >6 cms^{-1}) medium (green), and slow speeds (black, <3 cms^{-1}) were annotated.

Ciliary Motility Recording. High-resolution ciliary beat analysis was done using a Zeiss Axioscope attached to an IDT MotionPro ×4 high-speed camera. Movies were recorded at 500 frames per second (×1,000 magnification), and slow-motion playback of captured sequences allowed the determination of ciliary beat frequency and beat pattern. Ciliary beat frequency calculation was done by dividing the frame rate (500) by the number of frames elapsed for the observer to count five ciliary beat cycles, multiplied by 5 to convert to beats per second (Hz).

Otolith Crystal Polymorph Determination. Utricular otoliths were dissected and washed with deionized water for 5 min, as described (12). They were then boiled in 0.5 M solution of cobalt nitrate (7) (102536, Merck Millipore) for 4 min and photographed immediately thereafter. A total of 6 otoliths from three individuals were used for *coch bbs2* and *bbs9* and 20 otoliths were used for *cep290*.

Proteomic Analysis. Dissected utricular otoliths were decalcified overnight at 4 °C in 0.2 M ethylenediaminetetraacetic acid (EDTA) in 100 mM Tris pH 8.0. Four otoliths from two fish were used for each experiment. After overnight incubation in EDTA, a transparent structure remained at the bottom of the tube, representing the decalcified protein matrix of the otoliths, which was homogenized using a hand-held homogenizer (47747-370, VWR). The samples were subsequently centrifuged on a benchtop centrifuge at 4 °C for 30 min at 13,000 rpm. After centrifugation, a pellet becomes apparent at the bottom of the tube, and the supernatant was transferred into a new tube and mixed with an equal volume of 2× Laemmli buffer. This provided the soluble fraction of otolith proteins. The pellet was washed with cold acetone and centrifuged at 4 °C for 20 min at 13,000 rpm. Acetone was removed, and the pellet air dried for 15 min. A total of 20 μl of 2× Laemmli buffer was added to the tube and the pellet was homogenized with a pestle, providing insoluble fractions. Both soluble and insoluble fractions were heated to 95 °C for 10 min and loaded on a 10% sodium dodecyl sulphate–polyacrylamide gel electrophoresis (SDS-PAGE) gel along with a Spectra Multicolor prestained protein ladder (26623, ThermoFisher Scientific). Electrophoresis was performed at 100 V for 2 h using the Mini-Protean Tetra system (Bio-Rad), after which gel was washed with dH_2O for 20 min on an orbital shaker at room temperature and fixed overnight in a 40% methanol, 10% acetic acid, and 50% dH_20 solution. Fixation solution was replaced with Coomassie Brilliant Blue R staining solution (161-0436, Bio-Rad), and incubation continued on an orbital shaker for 4 h at room temperature. To destain, gel was placed in dH_2O and microwaved six times, 1 min each, followed by incubation for 30 min at 37 °C. Gel was photographed using a white light transilluminator. Individual bands were excised with a scalpel blade and mass spectrometry was performed at Harvard Medical School-Taplin Mass Spectrometry Facility.

Western Blotting. For Western blot analysis, two to three otoliths were used to obtain insoluble fraction as described in the section *Proteomic Analysis*. Alternatively, adult fish head was homogenized using the same homogenizer as described in the section *Proteomic Analysis* in ∼0.3 mL lysis buffer (40 mM Pipes, 100 mM $MgCl_2$, 50 mM EDTA, and 400 mM NaCl). For westerns of larvae, ∼100 larvae were homogenized using a pestle in radioimmunoprecipitation assay (RIPA) buffer. The homogenate was diluted in equal volume of 2× Laemmli buffer and heated to 95 °C for 5 min. Proteins were separated on 12% SDS-PAGE gel, transferred to nitrocellulose membrane (Amersham GE Healthcare), and stained with anti-Cochlin primary antibody (1:800 to 1,000, Proteintech, custom made) and anti-rabbit IgG, horseradish peroxidase (HRP) (1:10,000, Abcam, ab97051) secondary antibody. Membranes were incubated in Pierce ECL Western Blotting Substrate according to manufacturer's instructions. Staining was visualized using the ChemiDoc MP Imaging System (Bio-Rad).

Immunohistochemistry. Zebrafish larvae were cryosectioned and immunostained using standard protocols (12). For Cochlin, larvae were fixed in 4% PFA overnight at 4 °C and treated using an antigen-retrieval protocol (13) prior to sectioning and immunostaining. Dent's fixative overnight at 4 °C was used for Cep290 staining. The following primary antibodies and dilutions were used: anti-acetylated tubulin (1:500 to 1,000, Sigma, T6793); anti-Cochlin (1:1,000, Proteintech, custom made); ZO-1 (mouse) 1A12 (Invitrogen, Category [Cat.] 33-9100, dilution) (1:200); PKC zeta /aPKC (rabbit poly) (Santa Cruz Biotechnology, Cat sc-216, dilution [1:50]), Rab8a (Novus, clone 3G1, mouse monoclonal, 1:200), and Rab11 (Cell Signaling, D4F5, rabbit mAb, 1:200). Prior to imaging, sections were counterstained with DAPI for 30 min to visualize nuclei. Images were collected with an Olympus FV1200 confocal microscope equipped with a 40×, NA 1.0 or 60×, NA 1.42 oil lens. Red signals were converted to magenta using Photoshop.

Microscopy and Photography. To evaluate otolith shape, 1.5-dpf larvae were dechorionated, anesthetized in 0.168% wt/vol Tricaine (Sigma, E10521) in E3 media (14), positioned in 3% methylcellulose with the lateral side up, and photographed using Zeiss Axio Zoom V16 microscope and PlanNeoFluar 1×/0.25 FWD 56-mm lens. Alternatively, Zeiss Axio Observer inverted microscope and 20× NA 0.5 Plan NeoFluar lens was used.

Adult fish were photographed after being anesthetized in Tricaine diluted in aquarium water as described in this section. Animals were positioned with the lateral side up in plastic boats (VWR) filled with 20 mL Tricaine solution. Photographs were obtained using a 12-megapixel digital camera. For scanning electron microscopy, otoliths of adult individuals were dissected, washed in PBS for 10 min, fixed in 4% PFA overnight at 4 °C, and left in 1 mL 100% ethanol for 24 h in an open glass dish to allow ethanol evaporation. Larvae were fixed in 2.5% glutaraldehyde in 100 mM Na cacodylate buffer (pH 7.5) overnight, washed in buffer, 1 h postfixed in 2% OsO_4, washed again, and dehydrated in an ethanol series before drying in a mixture of 50% Hexamethyldisilazane (HEX) in 100% ethanol and final drying in 100% HEX. After removal of this solution, larvae were left to dry overnight in a fume hood. Dried larvae were broken using watchmaker's forceps under a stereomicroscope to expose the inner ear vesicle. If required, the otolith was removed. Adult otoliths or larvae were then immobilized on carbon adhesive discs mounted on scanning electron microscopy sample stubs, coated with gold using Edwards S150B Gold Sputter Coater, and imaged on Phillips XL-20 or Tescan Vega3 microscope.

In Situ Hybridization. The *cochlin* probe was synthesized using zebrafish cDNA clone obtained by Dharmacon (EDR5649-213361471) using standard protocols (14). Hybridization, washes, signal detection, and postfixation were carried out as published (15). For photography, larvae were positioned in 3% methycellulose and photographed using Axio Zoom Version 16 Zeiss microscope with a PlanNeoFluar 2.3×/0.57 FWD 10.6-mm lens. To study expression further, larvae were embedded in Epon using standard protocols (12) and sectioned at 10 μm on Reichert–Jung Ultracut E ultramicrotome. Sections were counterstained with DAPI and photographed using Zeiss Axio Observer inverted microscope and 100×, NA 1.4 oil lens.

Morpholino Knockdown. Morpholino knockdowns were performed as described previously (12, 16). *Coch* ATG: GGACAGCAAACCACAACGACATGGT, *coch* Sp: AAGTGAAAACTGTACCTGTGAATGG, and Control: CCTCTTACCTCAGTTACAATTTATA

Statistical Analysis. Statistical analysis was carried out using Student's *t* test, χ^2 test or Kruskal–Wallis test included in GraphPad Prism 7.0 software (http://www.graphpad.com/). Data are represented as mean ± 95% CI. Significance is represented as follows: $*P < 0.05$, $**P < 0.01$, $***P < 0.001$, and $****P < 0.0001$.

Results

The zebrafish *cep290*^{sa1383} mutant allele does not cause obvious developmental defects (Fig. 1*A*), and confirmed by sequencing, the correct mutation was present in the fish (Fig. 1 *B* and *C*). We noticed, however, that mutant larvae become hyperactive in response to osmotic shock (Fig. 1 *D* and *F*). Similarly, adult homozygotes swam more actively compared to wild-type controls (Fig. 1 *E* and *G*). To investigate whether this behavior is due to vestibular abnormalities, we dissected otoliths and analyzed them using SEM. In contrast to wild-type utricular otoliths, which have a smooth surface, mutant otoliths form sharp ridges (Fig. 2*A*). In the zebrafish embryo, two equally sized otoliths are developed on the second day of development (17, 18). Morphologically defective otoliths are also transiently present in *cep290*^{sa1383} embryos, where they are either strongly unequal in size or there are more than two otoliths present, often close together and perhaps in the process of fusion (Fig. 2 *B* and *C*). Otolith defects could be the result of defects in cilia formation or function in the ear; however, we were not able to detect such defects in *cep290*^{sa1383} larvae using various assays (*SI Appendix*, Fig. S1 and Movies S1 and S2).

Otolith morphology defects that we observed in *cep290* mutants suggested that calcium carbonate does not crystalize properly in the mutant strain. To determine whether $CaCO_3$ crystal polymorph is affected by *cep290*^{sa1383} mutations, we stained otoliths with cobalt nitrate (7). Mutant otoliths display more-intense brown staining (Fig. 2*D*), revealing increased aragonite content. This result shows that Cep290 functions in a process that regulates $CaCO_3$ crystallization.

Abnormal $CaCO_3$ crystallization suggested that secretion of otolith proteins by ear epithelia was affected in our *cep290*^{sa1383} allele. Electrophoretic analysis of protein content from wild-type and *cep290*^{sa1383} mutant otoliths revealed that, indeed, a prominent band of ca. 42 kDa is significantly reduced in the mutant (Fig. 3*A*, arrow). Based on mass spectrometry, we determined that the missing protein is Cochlin (*SI Appendix*, Fig. S2). Cochlin contains two von Willebrand Factor (vWF) domains and an N-terminal Limulus factor C, Cochlin, Lgl1 (LCCL) domain, homologous to a hemolymph coagulation factor (Fig. 3*B*) known to be proteolytically removed in some tissues (19, 20). The vWF domains are found in complement proteins and extracellular matrix components, including collagens. Cochlin fragments are secreted into bloodstream during inflammation (19). Secretion into the ear lumen has not been, however, reported thus far, possibly due to different protein-extraction methods used. The 42-kDa band that we identified in the otolith corresponds to the processed form of Cochlin with the LCCL domain removed (Fig. 3*A* and *SI Appendix*, Fig. S3).

Human missense mutations in Cochlin are associated with autosomal-dominant hearing loss (DFNA9) (19, 21). Consistent with otolithic defects, both human and mouse *cochlin* mutations result in vestibular malfunction (22, 23), which, in the mouse, precedes hearing loss (23). Human mutations also cause vertigo in some patients (22). Despite this, Cochlin presence in otoliths has not been previously reported.

To investigate Cochlin function further, we generated deletion alleles in each VWF domain (Fig. 3*B*). Similar to *cep290*^{sa1383} mutants, *coch*$^{-/-}$ mutant homozygotes and morphants display otolith defects at 36 h postfertilization (hpf) (Fig. 3*C* and *SI Appendix*, Fig. S4). *Coch* crispants also showed hyperactivity in response to osmotic shock (*SI Appendix*, Fig. S4*E*). Otoliths of adult *coch*$^{-/-}$ homozygotes form sharp crystals and display grossly abnormal shapes (Fig. 3*D* and *SI Appendix*, Fig. S5). Compared to *cep290*^{sa1383} mutants, these defects occur earlier and are more severe. Cobalt nitrate staining confirmed overabundance of aragonite in *coch*$^{-/-}$ otoliths (Fig. 3*E*). These findings show that Cochlin functions as a $CaCO_3$ crystallization determinant.

Cep290 physically interacts with proteins encoded by Bardet–Biedl Syndrome (BBS) genes, thought to be involved in intracellular transport (24–26). To test whether BBS proteins also affect Cochlin secretion, we characterized *bbs2*^{sa2952} and *bbs9*^{sa14425} mutants (Fig. 4 *A* and *D* and *SI Appendix*, Fig. S6). Both mutants display transient otolith defects at 36 hpf (Fig. 4 *B* and *E*). *bbs2*$^{+/-}$; *cep290*$^{sa1383/+}$ and *bbs9*$^{+/-}$; and *cep290*$^{sa1383/+}$ double heterozygous embryos also display otolith defects, revealing genetic interaction between *cep290* and *bbs* loci (Fig. 4 *C* and *F*). Scanning electron microscopy on otoliths from *bbs2*$^{-/-}$ adult homozygotes revealed somewhat abnormal crystallization (*SI Appendix*, Fig. S6). Moreover,

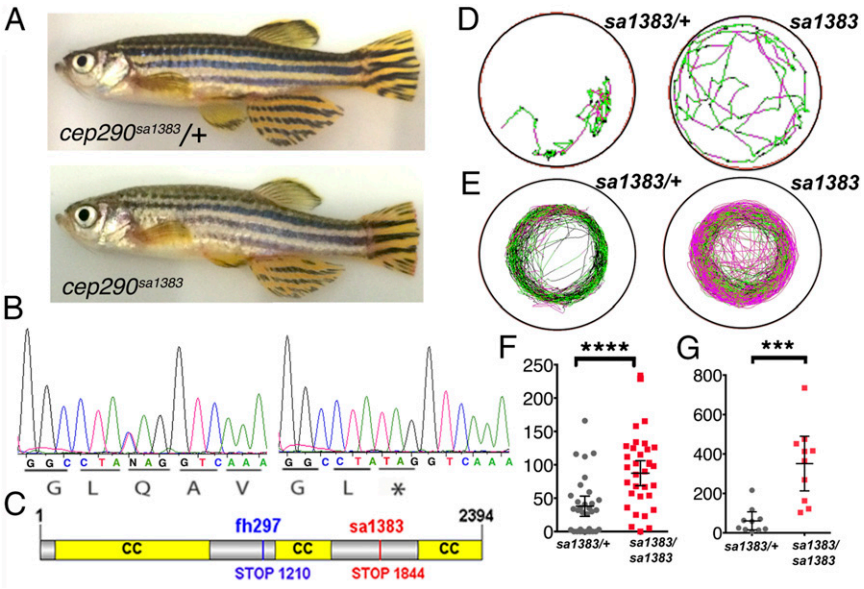

Fig. 1. *cep290* mutant phenotype. (*A*) Phenotype of homozygous *cep290*^{sa1383} adult fish. (*B*) Sequence of the *sa1383* mutant allele used in this study. (*C*) Cep290 domain structure showing mutations used in this study. (*D* and *E*) Example swimming tracks of heterozygote control (*Left*) and homozygous mutant (*Right*) larvae after osmotic shock (*D*) and adults (*E*); black represents slow movement or static, green represents medium, and red represents fast movement. (*F* and *G*) Total distance traveled for swimming trajectories (mm) such as ones shown in (*D* and *E*) for larvae after osmotic shock (*F*) and adults (*G*). ****P < 0.0001; ***P < 0.001; Student's t test; 95% CI.

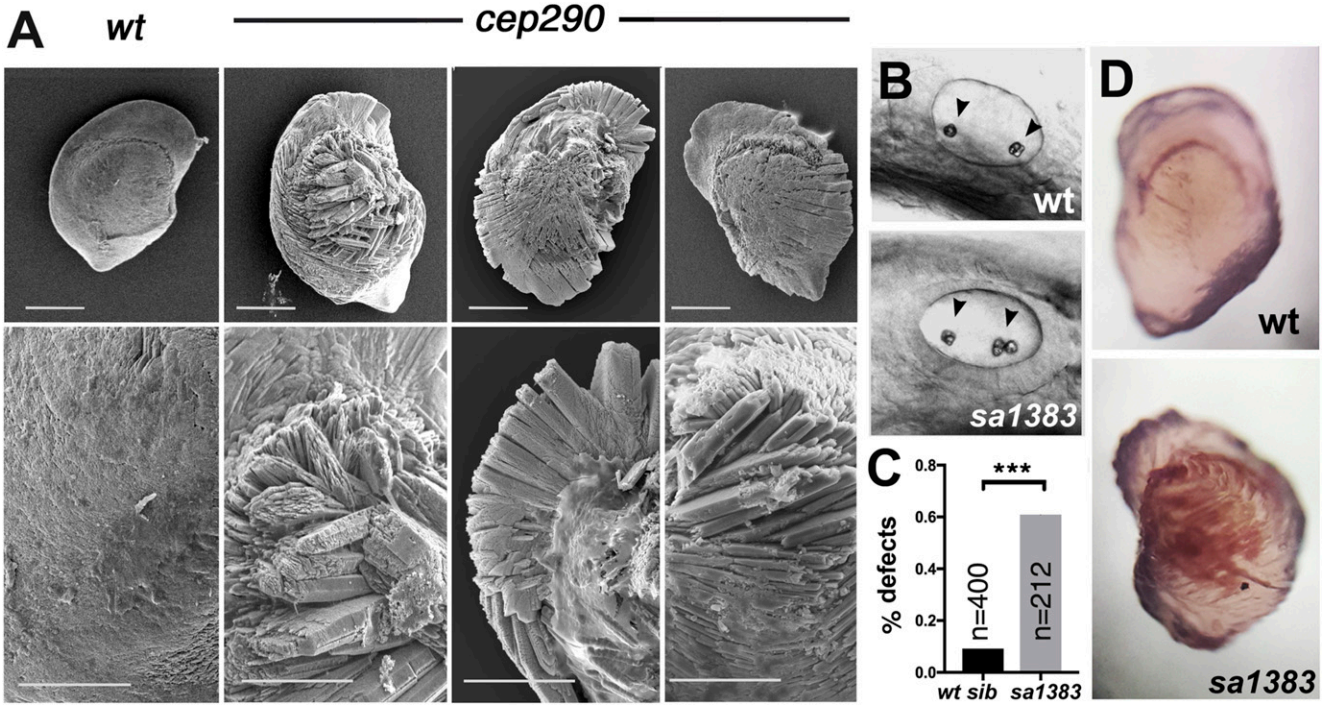

Fig. 2. Otolith crystallization defects in *cep290* mutant homozygotes. (*A*) Example scanning electron microscopy images of wild-type and *cep290*^{sa1383} otoliths at 18 mo (Scale bar, 300 μm). Enlargements in *Bottom* panels (Scale bar, 150 μm) ($n = 3$). (*B*) Side views of otic vesicles in live wild-type and *cep290*^{sa1383} homozygous embryos at 36 hpf. In the posterior ear, in the mutant example, two closely apposed otoliths are seen, where one is expected. Anterior is *Left*, dorsal *Up*, arrowheads indicate otoliths. (*C*) Frequency of otolith defects at 36 hpf. $P < 0.001$, χ^2 test. (*D*) Typical example of cobalt nitrate staining of utricular otoliths in wild-type and *cep290*^{sa1383} mutants ($n = 20$).

cobalt nitrate staining is more prominent in otoliths from these animals (Fig. 4*G*). By contrast, otoliths from *bbs9*$^{-/-}$ homozygotes display largely normal cobalt staining (Fig. 4*G*). These data show that Cep290 and its interaction partners first function transiently during embryogenesis in otolith formation and later in life facilitate Cochlin secretion and otolithic calcium carbonate crystallization.

To determine which cells secrete Cochlin, we first performed in situ hybridization on embryos and larvae. *Cochlin* transcript is expressed at a high level in the ear (*SI Appendix*, Fig. S7). On sections, high expression is visible at the anterior and medial edge of the utricular macula and at the dorsal and to a lesser extent ventral edge of the saccular macula (Fig. 5*A* and *SI Appendix*, Fig. S7). To localize Cochlin polypeptide, we performed antibody staining on sections through the ear. This analysis revealed high levels of Cochlin in small groups of cells immediately adjacent to sensory maculae but not in hair cells (Fig. 5 *B–D* and *SI Appendix*,

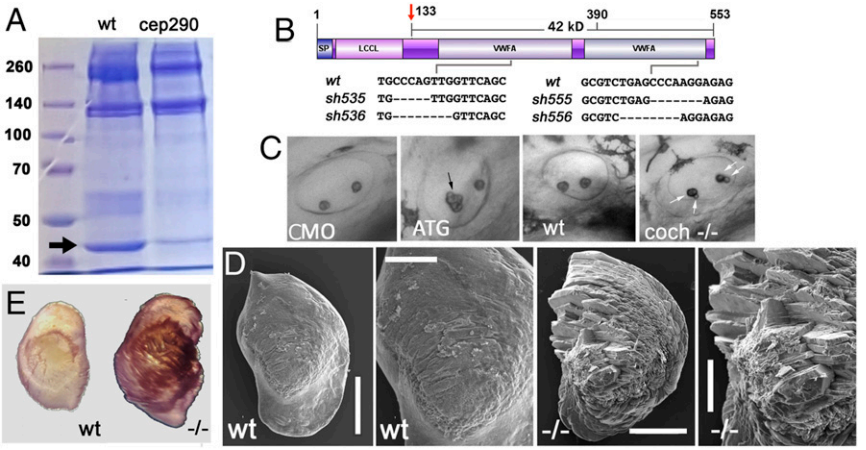

Fig. 3. Otolithic Cochlin deficiency in mutants of cilia genes and *cochlin* mutant phenotype. (*A*) Otolithic proteins from wild-type and *cep290*^{sa1383} homozygotes separated on a polyacrylamide gel and visualized with Coomassie blue staining. The arrow indicates Cochlin band. (*B*) Domain structure of the *cochlin* gene. LCCL, Limulus factor C, Cochlin, Lgl1 domain; vWF, von Willebrand Factor domains. Deletions in CRISPR-induced mutants are indicated. The antiserum against Cochlin was made against the C terminus (amino acids 390 to 553) (*C*) Otolith morphology in morphant and *coch*^{sh536} mutant embryos as indicated. ATG-targeted morpholino (ATG) was used. Shown are side views of otic vesicles in live embryos, the arrows point at otoliths that are abnormal. (*D*) Scanning electron microscopy images of typical otoliths from wild-type and *coch* ^{sh536} mutant adult at 7 mo of age (Scale bars, overview 300 μm, blow up 150 μm) ($n = 3$). (*E*) Example of cobalt nitrate staining of utricular otoliths from wild-type and *coch* ^{sh536} mutant at 7 mo ($n = 3$).

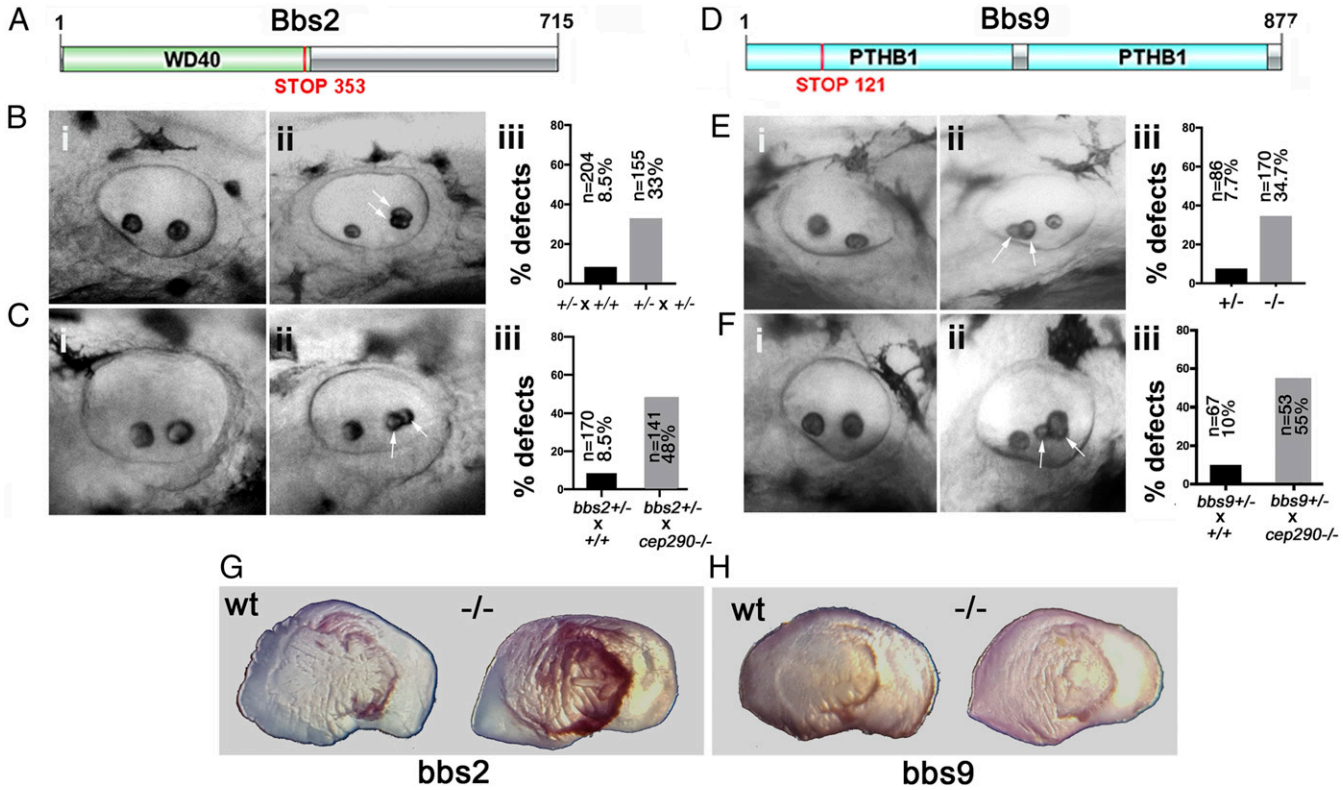

Fig. 4. Otolith phenotypes of BBS mutants and genetic interactions between *cep290* and *bbs* loci at 36 hpf. (*A* and *D*) Schematic representation of Bbs2 and Bbs9 protein domain structure. Sites of mutations in $bbs2^{sa2952}$ and $bbs9^{sa14425}$ alleles used in this study are indicated. (*B*), $bbs2^{-/-}$ mutant phenotype. Lateral views of otic vesicles from (*i*) $bbs2^{+/-}$ outcross to a wild-type strain and (*ii*) $bbs2^{+/-}$ incross. In (*ii*) an individual with abnormal otolith morphology is shown. (*iii*) Frequency of otolith defects in embryos originating from $bbs2^{+/-}$ outcross and incross. ($P < 0.0001$, χ^2 test) (*C*) Phenotype of embryos originating from $bbs2^{+/-}$ outcrosses to a wild-type and a cep290$^{-/-}$ strain. Lateral views of otic vesicles from (*i*) $bbs2^{+/-}$ outcross to a wild-type stain and (*ii*) $bbs2^{+/-}$ outcross to $cep290^{sa1383}$ homozygous strain. (*iii*) Frequency of otolith defects in $bbs2^{+/-}$ outcrosses. ($P < 0.0001$, χ^2 test). (*E*) Phenotype of $bbs9^{-/-}$ mutant homozygotes. Lateral views of the otic vesicle from (*i*) $bbs9^{+/-}$ heterozygote and (*ii*) $bbs9^{-/-}$ mutant homozygote with abnormal otolith number (3 instead of 2). (*iii*) Frequency of otolith defects in $bbs9^{-/-}$ homozygotes, compared to $bbs9^{+/-}$ heterozygotes ($P < 0.0001$, x^2 test). (*F*) Phenotype of embryos originating from $bbs9^{+/-}$ outcrosses to a wild-type and a cep290$^{-/-}$ strain. Lateral views of otic vesicles from (*i*) $bbs9^{+/-}$ outcross to a wild-type and (*ii*) $bbs9^{+/-}$ outcross to $cep290^{-/-}$ homozygous strain. (*iii*) Frequency of otolith defects in $bbs9^{+/-}$ outcrosses as above ($P < 0.0001$, χ^2 test). The arrows indicate abnormally forming otoliths. (*G*) Examples of cobalt nitrate staining of utricular otoliths from $bbs2^{-/-}$ (*H*) and $bbs9^{-/-}$ (*i*) mutants at 23 and 26 mo of age, respectively ($n = 3$).

Figs. S1 and S8). Consistent with its secretion and incorporation into the otolith, Cochlin signal accumulates in the apical cytoplasm of these cells (Fig. 5*D*, arrows). Cochlin is also abundantly present in the basal lamina of epithelia lining the ear cavity (Fig. 5 *B* and *C*, arrowheads). Compared to *cochlin* transcript, Cochlin protein is found over much larger area, indicating that it diffuses long distances along the basal surface of epithelia, or that cochlin expression may be more widespread at earlier stages.

While secretory vesicles of Cochlin accumulate apically in cells adjacent to sensory maculae of the wild-type ear, in $cep290^{sa1383}$ homozygotes, they are nearly entirely absent (Fig. 5 *E–H*, arrows). This phenotype is fully penetrant in the anterior macula (0/11 for mutants; 13/13 for wild-type). A similar phenotype is found in $bbs2^{-/-}$ mutants (0/9 versus 7/7, Fig. 5 *I* and *J*). Posterior macula phenotypes are less consistent. Combined with observations of Cochlin absence in mutant otoliths, these data show that *cep290* and *bbs2* determine the polarity of Cochlin secretion: in wild-type animals, Cochlin is secreted both apically and basally to be incorporated into the otolithic matrix and the basal lamina, respectively. By contrast, in $cep290^{sa1383}$ and $bbs2^{-/-}$ mutants, Cochlin secretion is directed basally. In contrast to hair cells, Cochlin-expressing cells do not, however, differentiate prominent cilia (Fig. 5*L*, *SI Appendix*, Fig. S1). Furthermore, $ovl/Ift88^{-/-}$ mutants do not affect Cochlin distribution in the cytoplasm, and we did not see clear defects in two important regulators of apical vesicle trafficking Rab11 and Rab8 in $cep290^{sa1383}$ mutants (*SI Appendix*, Fig. S9).

Discussion

Our analysis did not detect clear cilia phenotypes in $cep290^{sa1383}$ mutants, and our phenotypes were less severe than mouse *cep290* knockouts or zebrafish $cep290^{fh297}$ mutants; this might be because the *sa1383* allele leaves a substantial amount of protein intact. Additionally, we could not detect significant down-regulation of the mutant messenger RNA using qPCR and did not detect alternative splicing (*SI Appendix*, Fig. S10), suggesting a truncated protein could be produced. Although our analysis may have missed subtle cilia phenotypes, we consider it more likely that this allele identifies a unique phenotype of CEP290, in addition to functions for both Cochlin and a subset of ciliopathy genes. We show that Cochlin determines $CaCO_3$ crystallization, and its role in otolith crystallization may account for vestibular dysfunction associated with human *cochlin* mutations (20, 21). Importantly, the structural defect is only observed in the utricular otoliths, possibly due to the different crystal polymorph composition of the different otoliths. Moreover, Cochlin is enriched basally in sensory epithelia of Meniere's disease patients (27), suggesting that basal secretion defects of Cochlin may also be associated with balance disorders. It is noteworthy that mutations in Cochlin are mostly dominant missense mutations in the N-terminal Factor C homology

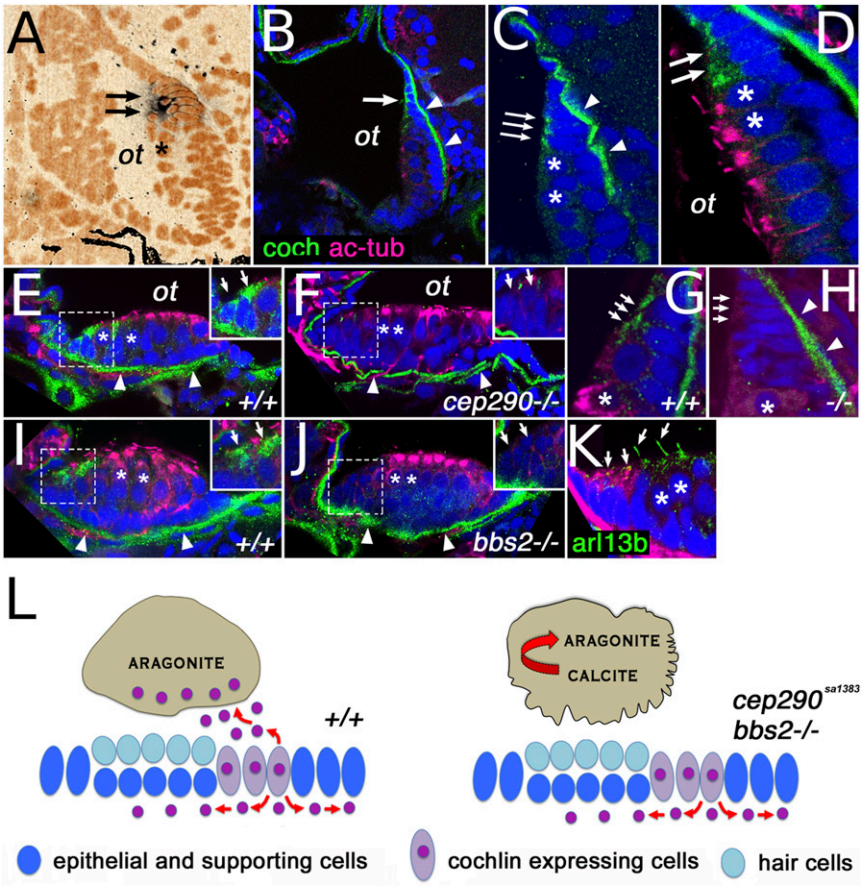

Fig. 5. Cochlin expression pattern. (*A*) *cochlin* transcript expression (arrows) in the posterior macula of the zebrafish otic vesicle at 5 dpf. (*B* and *C*) Cochlin protein expression (in green) in the posterior macula at 5 dpf. (*D*) Cochlin expression (in green, arrows) at the dorsal rim of the posterior macula in cells immediately adjacent to hair cells (asterisks). (*E–H*) Cochlin protein localization in anterior (*E* and *F*) and posterior (*G* and *H*) maculae of wild-type and *cep290*^{sa1383} homozygotes as indicated at 5 dpf. (*I* and *J*) Cochlin expression in the anterior macula of wild-type (*I*) and *bbs2*$^{-/-}$ mutants (*J*). (*K*) Cilia visualized with *Arl13b-GFP* transgene (in green, arrows), Cochlin in red. (*L*) Model of *cep290* and *bbs2* function in Cochlin secretion. Loss of *cep290*, *bbs2*, and most likely other cilia-related genes leads to defects apical Cochlin secretion into the ear lumen and causes abnormal crystallization of otolithic calcium carbonate. In (*D–K*), sections are double stained for acetylated tubulin (in magenta), which accumulates apically in hair cells. All sections are counterstained with DAPI in blue (pseudocolored in orange in *A*). *Insets* in (*E*, *F*, *I*, and *J*) show enlargements of Cochlin-secreting cells (enclosed in dashed line boxes). In (*B–J*), the arrows indicate Cochlin-secreting cells and the arrowheads point to Cochlin presence in the basal lamina. "ot" otolith position, asterisks indicate hair cells. $CaCO_3$ crystal structure after ref. 36.

domain and lead to a form of Cochlin that is secreted but forms deposits in the vestibular and cochlear labyrinths (20, 21). More recently, a form of recessive hearing loss (DFNB110) has been attributed to loss-of-function mutations in Cochlin, similar to the mutations we have generated, and vestibular dysfunction was also reported (28), consistent with our observations.

CEP290 interacts with the BBS complex, which itself is required for interflagellar transport (IFT) particle assembly and transport. The fact that *ovl* (*ift88*) mutants do not show Cochlin secretion defects is interesting but consistent with reports that the BBSome has roles in vesicular transport that do not involve cilia. For instance, melanosome transport (29) and Notch receptor recycling to the membrane have been reported (30). Especially the latter suggests that the specific delivery of "Cochlin cargo" to the plasma membrane by the BBSome is an interesting possibility. It is also worth pointing out that *cep290*^{sa1383} and *bbs2*$^{-/-}$ mutants are possibly promising models for slow, age-related degenerative diseases of the human vestibular system. Few such models are available, although they are potentially useful in drug screening efforts.

These results show that ciliary proteins have the ability to act as key regulators of secretory polarity in epithelia. Although epithelial polarity defects have not been reported in vertebrate cilia mutants prior to this analysis (see for example refs. 31 and 32), several studies suggested that ciliogenesis and cell polarity are interconnected. For example, some Nephrocystins interact physically with epithelial polarity determinants Stardust/Pals1 and Par6 (33). Similarly, the Par3/Par6/aPKC complex and Crumbs proteins were shown to contribute to ciliogenesis (34, 35), and several Nephrocystins contribute to tight junction formation in cell culture spheroids (32). We present in vivo evidence showing that cilia genes facilitate apical secretion and function as potent determinants of secretion polarity (summarized in Fig. 5*L*). Such a function could be mediated via cytoskeletal elements or by providing secretory vesicle docking sites. Secretion defects reported in this study reveal a role for cilia genes and suggest that they may regulate secretory processes in other organs and tissues, thus contributing to clinical manifestations of human ciliopathies which have gone unnoticed thus far.

Data Availability. All study data are included in the article and/or supporting information.

ACKNOWLEDGMENTS. We thank Profs. Holley, Johnson, Peden, Marcotti, and Smythe for helpful suggestions at various stages of this project. We thank the aquarium staff, the Zebrafish Behavioural Unit, and the electron microscopy facility at the University of Sheffield for their support. This work was supported by the Biotechnology and Biological Sciences Research Council (Grant Numbers: BB/R005192/1; BB/R015457/1) and the Medical Research Council (Grant Number: MR/N000714/1).

1. D. A. Parfitt *et al*., Identification and correction of mechanisms underlying inherited blindness in human iPSC-derived optic cups. *Cell Stem Cell* **18**, 769–781 (2016).
2. F. Coppieters, S. Lefever, B. P. Leroy, E. De Baere, CEP290, a gene with many faces: Mutation overview and presentation of CEP290base. *Hum. Mutat.* **31**, 1097–1108 (2010).
3. H. Straka, A. Zwergal, K. E. Cullen, Vestibular animal models: Contributions to understanding physiology and disease. *J. Neurol.* **263** (suppl. 1), S10–S23 (2016).
4. S. Fermani, S. Vanzo, M. Miletic, G. Zaffino, Influence on the formation of aragonite or vaterite by otolith macromolecules. *Eur. J. Inorg. Chem.* **2005**, 162–167 (2005).
5. R. Dongni, G. Yonghua, F. Qingling, Comparative study on nano-mechanics and thermodynamics of fish otoliths. *Mater. Sci. Eng. C* **33**, 9–14 (2013).
6. C. Söllner *et al*., Control of crystal size and lattice formation by starmaker in otolith biomineralization. *Science* **302**, 282–286 (2003).
7. J. Weigele, T. A. Franz-Odendaal, R. Hilbig, Not all inner ears are the same: Otolith matrix proteins in the inner ear of sub-adult cichlid fish, oreochromis mossambicus, reveal insights into the biomineralization process. *Anat. Rec. (Hoboken)* **299**, 234–245 (2016).
8. G. Ishiyama, I. A. Lopez, A. R. Sepahdari, A. Ishiyama, Meniere's disease: Histopathology, cytochemistry, and imaging. *Ann. N. Y. Acad. Sci.* **1343**, 49–57 (2015).
9. I. S. Curthoys, L. Manzari, Otolithic disease: Clinical features and the role of vestibular evoked myogenic potentials. *Semin. Neurol.* **33**, 231–237 (2013).
10. M. Tsujikawa, J. Malicki, Intraflagellar transport genes are essential for differentiation and survival of vertebrate sensory neurons. *Neuron* **42**, 703–716 (2004).
11. K. J. Clark, N. J. Boczek, S. C. Ekker, Stressing zebrafish for behavioral genetics. *Rev. Neurosci.* **22**, 49–62 (2011).
12. E. Leventea, K. Hazime, C. Zhao, J. Malicki, Analysis of cilia structure and function in zebrafish. *Methods Cell Biol.* **133**, 179–227 (2016).
13. D. Inoue, J. Wittbrodt, One for all—A highly efficient and versatile method for fluorescent immunostaining in fish embryos. *PLoS One* **6**, e19713 (2011).
14. B. Thisse *et al*., Spatial and temporal expression of the zebrafish genome by large-scale in situ hybridization screening. *Methods Cell Biol.* **77**, 505–519 (2004).
15. M. Gering, R. Patient, Hedgehog signaling is required for adult blood stem cell formation in zebrafish embryos. *Dev. Cell* **8**, 389–400 (2005).
16. J. Malicki, H. Jo, X. Wei, M. Hsiung, Z. Pujic, Analysis of gene function in the zebrafish retina. *Methods* **28**, 427–438 (2002).
17. T. T. Whitfield, Cilia in the developing zebrafish ear. *Philos. Trans. R. Soc. Lond. B Biol. Sci.* **375**, 20190163 (2020).
18. B. B. Riley, C. Zhu, C. Janetopoulos, K. J. Aufderheide, A critical period of ear development controlled by distinct populations of ciliated cells in the zebrafish. *Dev. Biol.* **191**, 191–201 (1997).
19. B. F. Py *et al*., Cochlin produced by follicular dendritic cells promotes antibacterial innate immunity. *Immunity* **38**, 1063–1072 (2013).
20. N. G. Robertson, S. A. Hamaker, V. Patriub, J. C. Aster, C. C. Morton, Subcellular localisation, secretion, and post-translational processing of normal cochlin, and of mutants causing the sensorineural deafness and vestibular disorder, DFNA9. *J. Med. Genet.* **40**, 479–486 (2003).
21. N. G. Robertson *et al*., Mutations in a novel cochlear gene cause DFNA9, a human nonsyndromic deafness with vestibular dysfunction. *Nat. Genet.* **20**, 299–303 (1998).
22. U. Khetarpal, H. F. Schuknecht, R. R. Gacek, L. B. Holmes, Autosomal dominant sensorineural hearing loss. Pedigrees, audiologic findings, and temporal bone findings in two kindreds. *Arch. Otolaryngol. Head Neck Surg.* **117**, 1032–1042 (1991).
23. S. M. Jones *et al*., Hearing and vestibular deficits in the Coch(–/–) null mouse model: Comparison to the Coch(G88E/G88E) mouse and to DFNA9 hearing and balance disorder. *Hear. Res.* **272**, 42–48 (2011).
24. Y. Zhang *et al*., BBS mutations modify phenotypic expression of CEP290-related ciliopathies. *Hum. Mol. Genet.* **23**, 40–51 (2014).
25. T. R. Stowe, C. J. Wilkinson, A. Iqbal, T. Stearns, The centriolar satellite proteins Cep72 and Cep290 interact and are required for recruitment of BBS proteins to the cilium. *Mol. Biol. Cell* **23**, 3322–3335 (2012).
26. H. Jin *et al*., The conserved Bardet-Biedl syndrome proteins assemble a coat that traffics membrane proteins to cilia. *Cell* **141**, 1208–1219 (2010).
27. A. P. Calzada, I. A. Lopez, L. Beltran Parrazal, A. Ishiyama, G. Ishiyama, Cochlin expression in vestibular endorgans obtained from patients with Meniere's disease. *Cell Tissue Res.* **350**, 373–384 (2012).
28. S. P. F. JanssensdeVarebeke *et al*., Bi-allelic inactivating variants in the COCH gene cause autosomal recessive prelingual hearing impairment. *Eur. J. Hum. Genet.* **26**, 587–591 (2018).
29. H. J. Yen *et al*., Bardet-Biedl syndrome genes are important in retrograde intracellular trafficking and Kupffer's vesicle cilia function. *Hum. Mol. Genet.* **15**, 667–677 (2006).
30. C. C. Leitch, S. Lodh, V. Prieto-Echagüe, J. L. Badano, N. A. Zaghloul, Basal body proteins regulate Notch signaling through endosomal trafficking. *J. Cell Sci.* **127**, 2407–2419 (2014).
31. Y. Omori *et al*., Elipsa is an early determinant of ciliogenesis that links the IFT particle to membrane-associated small GTPase Rab8. *Nat. Cell Biol.* **10**, 437–444 (2008).
32. L. Sang *et al*., Mapping the NPHP-JBTS-MKS protein network reveals ciliopathy disease genes and pathways. *Cell* **145**, 513–528 (2011).
33. M. Delous *et al*., Nephrocystin-1 and nephrocystin-4 are required for epithelial morphogenesis and associate with PALS1/PATJ and Par6. *Hum. Mol. Genet.* **18**, 4711–4723 (2009).
34. S. Fan *et al*., Polarity proteins control ciliogenesis via kinesin motor interactions. *Curr. Biol.* **14**, 1451–1461 (2004).
35. K. Hazime, J. J. Malicki, Apico-basal polarity determinants encoded by *crumbs* genes affect ciliary shaft protein composition, IFT movement dynamics, and cilia length. *Genetics* **207**, 1041–1051 (2017).
36. V. Blanco-Gutierrez, A. Demourgues, V. Jubera, M. Gaudon, Eu(iii)/Eu(ii)-doped (Ca0.7Sr0.3)CO3 phosphors with vaterite/calcite/aragonite forms as shock/temperature detectors. *J. Mater. Chem. C Mater. Opt. Electron. Devices* **2**, 9969–9977 (2014).